Valence tautomerism, non-innocence, and emergent magnetic phenomena in lanthanide-organic tessellations

Maja A. Dunstan* and Kasper S. Pedersen*

Coordination networks based on lanthanide ions entangle collective magnetic phenomena, otherwise only observed in inorganic 4*f* materials, and the tunable spatial and electronic structure engineering intrinsic to coordination chemistry. We discuss the use of 2D-structure-directing linear $\{Ln^{II/III}I_2\}$ nodes to direct the formation of polymeric coordination networks. The equatorial coordination plasticity of $\{Ln^{II/III}I_2\}$ results in broad structural diversity, including previously unobtainable tessellations containing motifs observed in quasicrystalline tilings. The new phases host also magnetic frustration, which is at the origin of enhanced magnetic refrigeration potential. Finally, careful redox matching of *Ln* node and frontier orbitals of the ligand scaffold has culminated in the discovery of quantitative valence tautomeric conversion in a molecule-based *Ln* material, opening up new avenues for combining exotic magnetic phenomena with an encoded switch.

1. Introduction

Switchable materials, which exhibit disparate chemical and physical properties across multiple states, are necessary for applications that leverage changes in electronic, magnetic, or optical characteristics. Many such materials exist, both molecule-based and purely inorganic, including those where the electronic state can be manipulated and controlled by a stimulus such as temperature or pressure.[1] These encompass phenomena such as spin-crossover (SCO), between high-spin (hs) and low-spin (ls) *tautomers* of a transition metal ion;[2] stimulated intramolecular electron transfer between two metal ions; and *valence tautomerism* (VT), involving stimulated intramolecular electron transfer between a redox-active metal ion and a redox-active ligand (Fig. 1).[3,4] For SCO and VT materials, the vast majority of research has focused on coordination complexes of the 3*d* metal ions, for which there are known sets of metal ions and ligand scaffolds leading to facile switching by mild stimuli, such as temperature, pressure, and light.

VT transitions have been observed in coordination compounds of Mn,[5] Fe,[6] Co,[7,8,9] Cu,[10] Sn,[11] V,[12] amongst others, although most widely researched is the Co-dioxolene family of compounds (Fig. 1). Buchanan and Pierpont first observed the molecule-based VT phenomenon in 1980 in [Co(2,2′-bpy)(dbsq)(dbdiox)] (3,5-dbsq = 3,5-di-*tert*-butyl semiquinone, 3,5-dbdiox = 3,5-di-*tert*-butyl dioxolene, 2,2′-bpy = 2,2′-bipyridine), which hosts a thermally driven transition between a high-temperature (HT) Co^{II}-dbsq-dbsq tautomer and low-temperature (LT) Co^{III}-dbsq-dbq (dbq = 3,5-di-*tert*-butyl quinone) tautomer.[13] Progress in the proceeding 40 years has led to the observation of VT switching induced by various additional stimuli such as light,[14,15,16] pressure,[17,18] and X-rays.[13,19] Immobilization of VT complexes on surfaces[20] or on gold nanoparticles[21] has also been achieved for Co-dioxolene systems, with the possibility of now isolating single molecules as molecular switches. For many applications, cooperativity is key, leading to an abrupt SCO or VT transition upon an applied stimulus. In molecular materials, cooperativity in the solid-state bulk material is dictated by the crystal packing, which is difficult or impossible to design for molecular complexes. Instead, incorporation of switchable modules into coordination polymers or metal-organic frameworks (MOFs) is a tactic for engendering cooperativity. For SCO, multidimensional coordination networks have been widely explored since the 1990s, when Kahn *et al*. demonstrated cooperative, hysteretic SCO

Maja A. Dunstan is from Melbourne, Australia, and completed her PhD in the group of Colette Boskovic at the University of Melbourne. In 2022, she joined Kasper S. Pedersen at the Technical University of Copenhagen as a postdoctoral researcher. Her research interests include single-molecule magnetism, neutron spectroscopy, and switchable magnetic materials. Currently, she is working in the field of low-valent lanthanide coordination networks.

Kasper S. Pedersen was born in Allerød, Denmark, and received his PhD from the University of Copenhagen in 2014. After postdoctoral stints in Bordeaux and Montreal, he joined the faculty at the Technical University of Denmark in 2017, and was appointed full professor in 2022. His research spans synthetic and structural inorganic chemistry as well as advanced properties characterization. His current focus is directed toward the discovery of novel metal-organic framework materials with hitherto unknown structural and physical properties, and the development of the field of low/zero-valent metal cluster-based MOFs and the application of 3D electron diffraction techniques.

[a] *Department of Chemistry, Technical University of Denmark, DK-2800 Kgs. Lyngby, Denmark. E-mail: majdu@kemi.dtu.dk (M.A.D.), kastp@kemi.dtu.dk (K.S.P.)*

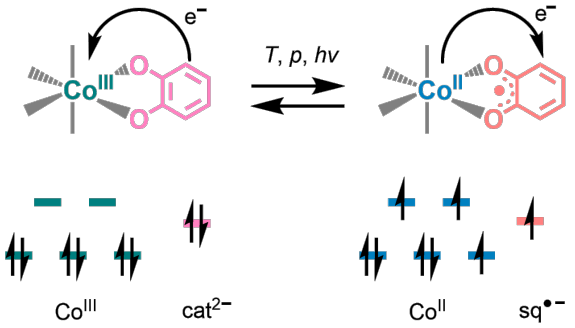

Fig. 1. Valence tautomeric process in an octahedral Co-dioxolene species, with a transition between a Co^{III}-catecholate ⇄ Co^{II}-semiquinonate. Occupation of metal 3*d* (teal/blue) and ligand (pink) valence orbitals shown.

switching in Fe^{II} 1D coordination polymers at room temperature.[22,23]Aside from the possibility of tuning both transition temperature and cooperativity, SCO coordination networks can also host multi-step transitions, where multiple states are accessible.[24,25] These materials also exhibit additional advantages over molecular complexes, for example where guest molecule–framework interactions induce a SCO transition.[26,27,28] In contrast, examples of VT coordination networks incorporating Co-dioxolene units typically show gradual transitions, with a strong sensitivity to desolvation[29,30,31] and guest molecule interactions.[32] One notable exception is the 2D coordination network $[Mn_2(NITIm)_3]ClO_4$ (NITImH = 2-(2-imidazolyl)-4,4,5,5-tetramethyl-4,5-dihydro-1*H*-3-oxide-1-oxyl), which shows a sharp thermal VT transition at room temperature with a thermal hysteresis of 20 K.[33] This observation hints that with a suitable combination of metal ion and ligand scaffold, extended networks exhibiting VT transitions could parallel the robust bistability found in SCO materials. However, for VT materials, unlike SCO materials, the concerted change in electronic structure of both the metal ion and the ligand scaffold may result in a highly correlated state existing in close energetic proximity to a diamagnetic or localised magnetic state. In extended networks, such correlations extend beyond the length scale of the molecule and will be at the origin of novel electronic and magnetic phases.

The VT transition is an entropically driven process. In Co-dioxolene compounds specifically, the entropy gain in the paramagnetic, HT Co^{II}-sq form is due to the larger spin state degeneracy leading to a gain in *electronic* entropy, as well as the longer metal-ligand bond lengths, leading to a higher density of vibrational states and a larger *vibrational* entropy. The thermal equilibrium is therefore determined by the Gibbs free energy, $\Delta G = \Delta H - T\,\Delta S$. According to this, the transition will occur when $\Delta G = 0$ and $\Delta H = T_c\Delta S$, which also defines the critical temperature, T_c.[34] Substitution of the dioxolene ligands has allowed for controlled tuning of the ligand redox potential, while careful choice in auxiliary ligand allows for tuning of the Co^{II}/Co^{III} redox couple, both directly modifying ΔH.[35] In addition, both solvent effects in solution state[36] and crystal packing effects[37] in the solid state affect the observed transition.

In stark contrast to transition metal ions, the lanthanide (*Ln*) ions are almost exclusively found as the trivalent ions with $4f^n$ electronic configurations and are typically considered redox innocent. For most Ln^{III} ions, unquenched orbital angular momentum and significant spin-orbit coupling dominate the electronic properties, with the crystal field effect of the ligand scaffold being only weak. One consequence of the unique electronic structure of the Ln^{III} ions is often large magnetic moments with strong magnetic anisotropy, leading to widespread technological applications in hard magnets (e.g., $SmCo_5$, $Nd_2Fe_{14}B$[38]) or potential future applications in single-molecule magnets.[39,40,41] Even in the case of negligible magnetic anisotropy, such as for $4f^7$ ions, e.g., Gd^{III}, the large magnetic moment has led to its use in MRI contrast agents[42] and in low-temperature magnetocaloric materials.[43] On the other hand, the weak crystal field interaction with the coordination environment gives rise to sharp, long-lived luminescence, which is used in, e.g., phosphors, sensors, and luminescent thermometers.[44] As these phenomena are intimately linked to the electronic configuration of the Ln^{III} ions, any change in oxidation state necessarily leads to a dramatic change in properties. In other words, manipulation of the oxidation state by a VT transition could allow for any of these properties to be switchable by an external stimulus.

In this Feature Article, we discuss the emergence of VT transitions in extended coordination networks based on *Ln* ions. First, the known redox properties of *Ln* species are briefly discussed, which are central to fluxional valence phenomena in lanthanide inorganic solid-state materials, as well as VT and intermediate valence tautomerism in molecular *Ln* materials. We then outline the work we have recently undertaken in the field of *Ln*-based coordination networks, which includes observation of novel geometric tessellations, slow magnetic relaxation, and enhanced sub-Kelvin magnetic refrigeration. This work culminates in the recent discovery of a samarium–pyrazine framework featuring a thermally activated and complete VT transition.

2. Frozen oxidation states

The lanthanide ions are by far most common in their trivalent state, with notable exceptions to this rule exhibiting either a closed-shell or half-filled 4*f* configuration: Ce^{IV} ($4f^0$), Eu^{II} ($4f^7$), and Yb^{II} ($4f^{14}$). Despite this redox-inactivity, synthetic efforts, primarily in the last decade, have now resulted in the isolation of Ln^{II} compounds for all *Ln* except Pm,[45,46,47,48] and Ln^{IV} coordination compounds for Ce,[49,50,51] Pr,[52,53] and Tb.[54,55] The implications for coordination chemistry utilising the Ln^{III}/Ln^{II} and Ln^{IV}/Ln^{III} redox couples have been reviewed by others.[56,57] Of the divalent *Ln* ions), Sm, Eu, and Yb are most stable towards oxidation to their trivalent state (Table 1), and simple precursors are commercially available. Eu^{II}, in particular, is widely used in inorganic phosphors, exhibiting tunable $4f^7 \leftarrow 4f^6$5d emission in the visible spectrum.[58] In the

Table 1. Standard reduction potentials ($E_{1/2}$ vs NHE) of Ln^{III}/Ln^{II} redox couples for selected *Ln*.[59]

	Nd	Sm	Eu	Dy	Tm	Yb
$E_{1/2}(Ln^{III}/Ln^{II})$ / V	−2.6	−1.5	−0.34	−2.6	−2.2	−1.2

field of molecular magnetism, organometallic complexes of Tb^{II} and Dy^{II} have shown promise as improved single-molecule magnets.[60] Synthetically, Ln^{II} ions are widely used as one-electron reducing agents[61] or more recently, as catalysts,[62,63] leveraging their large and negative reduction potentials. SmI_2, specifically, is widely used as a versatile, strong one-electron reductant for diverse organic transformations.[64,65]

Redox activity in molecular systems containing *Ln* ions is not necessarily limited to the metal centre itself, but could involve the ligand scaffold – a situation of great interest in the field of molecular magnetism. Such resulting radical ligand systems have been a synthetic target in the field of single-molecule magnets (SMMs), compounds which exhibit magnetic bistability at low temperatures.[66] In such systems, a strong magnetic anisotropy leads to an energy barrier to magnetization reversal and a wide magnetic hysteresis. This field was dominated by 3*d*-based polynuclear complexes, until Ishikawa *et al*. reported that the *Ln* complex $[Tb^{III}(Pc)_2]^-$ (Pc = phthalocyaninate) exhibited the same slow magnetic relaxation as the polynuclear complex-based SMMs.[67] In the proceeding 20 years, this has led to the discovery of SMMs with record breaking working temperatures.[39-41]

Further improving the performance of *Ln*-SMMs via coupling of electronic spins in polynuclear assemblies, akin to the strategy pursued for the 3d metal ion complexes, has been of limited success. The problem is rooted in the shielded nature of the 4*f* orbitals, that hinders any strong magnetic interaction between *Ln* ions in a given material. Ligand-based radicals often possess significant electronic spin densities at the ligating atom, thereby promoting the strong magnetic interactions in *Ln*-radical systems. Notable examples include the N_2^{3-}-bridged *Ln* dinuclear complexes, which show some of the highest hysteresis temperatures and, notably, extremely large magnetic coercivities.[68,69,70] The group of Murugesu recently published tetranuclear complexes, $[(Cp^*_2Ln^{III})_4(tz^{\bullet-})_4]$ (Cp* = pentamethylcyclopentadienide), consisting of $Cp^*_2Ln^{III}$ units bridged by tetrazine ($tz^{\bullet-}$) anion radical ligands. Here, strong magnetic exchange coupling leads to a large coercive field of H_{coer} = 3 T at 1.8 K.[71] Switching to a pyrazine anion radical ligand ($pyz^{\bullet-}$), the related family of compounds $[(Cp^*_2Ln^{III})_4(pyz^{\bullet-})_4]$ could be obtained.[72] Here, a coercive field of 6.5 T is observed for the Dy analogue. The extraordinary properties stem from strong *Ln*–radical magnetic exchange coupling, combined with a strongly axial crystal field at each Dy^{III} ion. Despite the potential of such scenarios for generating novel magnetic phases in coordination networks, these are yet to be discovered.

3. Redox isomerism and related phenomena in lanthanide materials

3.1 The dawn of VT transitions in lanthanide materials

Divalent *Ln* ions were first widely observed in inorganic solids. Perhaps unsurprisingly, valence change transitions have therefore been observed in intermetallics, chalcogenides, and oxides for all the common Ln^{II} ions. These transitions are typically characterised by (partial) electron transfer from the 4*f* orbitals to a conduction band, formally corresponding to an increase in the *Ln* oxidation state. Conceptually, this situation is analogous to the previously discussed VT transition, while commonly referred to as a valence change transition or valence instability. The first observation in 1912 of such a transition was in metallic Ce.[73] Herein, Ce exhibits a temperature- and pressure-dependent change in oxidation state from Ce^{III} to an intermediate valence $Ce^{3.6+}$ phase, due to the promotion of

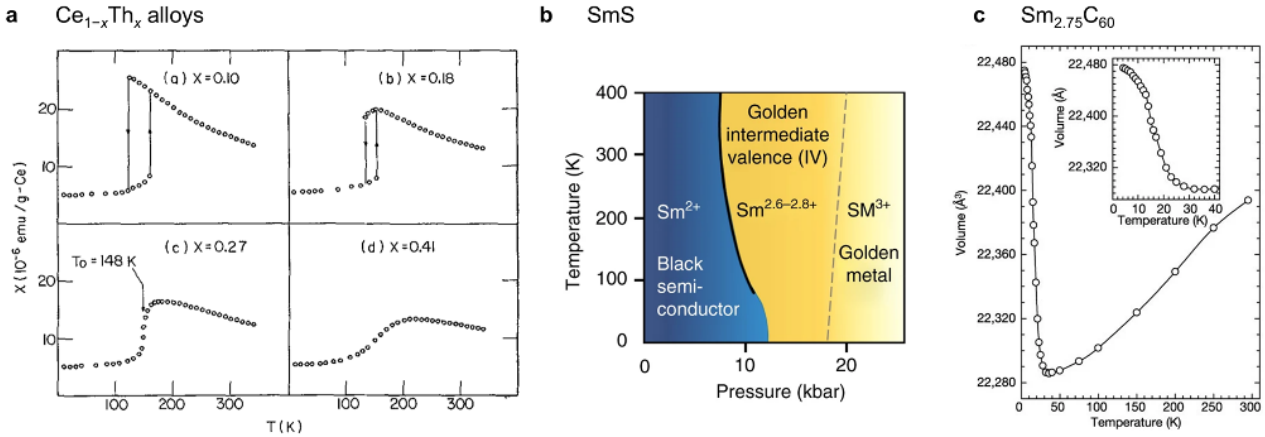

Fig. 2. (**a**) Temperature-dependent magnetic susceptibility (χ) in $Ce_{1-x}Th_x$ alloys exhibiting thermally induced valence transitions. Reproduced with permission from ref. 78. (**b**) Phase diagram of SmS redox tautomers, showing temperature- and pressure-dependent valence transitions. Reproduced from ref. 74. (**c**) Temperature dependence of the unit cell volume of $Sm_{2.75}C_{60}$, demonstrating the large negative thermal expansion driven by the valence transition. Reproduced with permission from ref. 86.

localised 4*f* electrons to the *s*-*d* conduction band.[72,75,76,77] Alloying with Th yields $Ce_{1-x}Th_x$ phases exhibiting thermally driven VT transitions, allowing for tuning of the transition temperature and pressure, with a cooperativity governed by the Th content (Fig. 2a).[78] Similarly, in samarium monosulfide, a pressure-induced (0.65 GPa) VT transition promotes an electron from Sm^{II} to the conduction band, giving a formal oxidation state of near 2.6+ in the "golden" intermediate-valence phase (Fig. 2b).[79,80] This transition is accompanied by a dramatic change in the physical properties, reflected in the semiconductor-to-metal transition. Even larger pressures lead to a complete transition to Sm^{III}, resulting in a metallic, correlated heavy fermion phase.[81] Chemical alloying of SmS with Y, Eu, Gd, or Yb leads to a shift in the temperature and pressure at which the valence transition occurs, analogous to the shift in the thermally induced transition in $Ce_{1-x}Th_x$ alloys.[82,83,84] For example, $Sm_{1-x}Y_xS$, stabilises the golden phase due to the "chemical pressure" from the dopant, and by x = 0.2, the intermediate valence state is observed at ambient pressure and room temperature.[85]

Lanthanide fullerides similarly exhibit VT transitions stimulated by temperature or pressure. In these compounds, *Ln* ions are intercalated between fulleride anions. Due to the molecular nature of the fullerides, the electron-accepting state is not necessarily the conduction-band, but could be of isolated, molecular origin. At room temperature, $Sm_{2.75}C_{60}$ is intermediate valence, with a Sm valence of 2.3+.[86] Upon decreasing temperature, a VT transition at 32 K leads to a localised Sm^{II} state, accompanied by a negative thermal expansion due to the increased ionic radius (Fig. 2c). Here, the electronic driving force for the VT transition is the thermal population of the low-lying t_{1u} level of C_{60} upon heating, leading to an overall decrease in occupation of the Sm 4*f* orbitals. An analogous VT transition is observed in the Yb congener, $Yb_{2.75}C_{60}$, with a higher transition temperature of 60 K.[87] A room-temperature, pressure-induced (4 GPa) VT transition is also observed for $Sm_{2.75}C_{60}$, which leads to the more intuitively expected increase in valency to Sm^{III}, driven by the smaller radius of the higher oxidation state ion.[88] Indeed, VT transitions are now widespread in inorganic solids, in particular in intermetallics.[89,90,91,92,93] Herein, the VT transitions are accompanied by stark changes in structural, electronic, magnetic, and optical properties.

3.2 Valence instabilities and nebulous oxidation states

In molecular *Ln* materials, observation of VT transitions is extremely limited. In 2009, Fedushkin *et al*. reported the observation of an in-solution VT transition in [(dpp-bian)Yb(dme)(μ-Br)]$_2$ (dpp-bian = 1,2-bis[(2,6-diisopropylphenyl)imino]-acenaphthene; dme = dimethoxyethane).[94] Here, a HT tautomer was observed to interconvert with a LT tautomer above room temperature. This was followed in 2012 by the observation of a VT transition in the compound [(dpp-bian)Yb(dme)(μ-Cl)]$_2$ (Fig. 3a) in solid state.[95] Single-crystal X-ray diffraction allowed the authors to conclude that one half of the dimer undergoes a VT transition–i.e. a LT-{$Yb^{III}_2(bian^{2-})_2$} ⇄ HT-{$Yb^{III}Yb^{II}(bian^{2-})(bian^{\bullet-})$} conversion (Fig. 3b). For this compound, only a single polymorph undergoes the VT transition, which hints that the tautomerism is particularly dependent on steric effects. This year, a gradual VT transition in the related, monomeric complex [(Ar^{BIG}-bian)Yb{(C(S)NMe_2)(dme)] (Ar^{BIG}-bian = 1,2-bis[(2,6-dibenzhydryl-4-methylphenyl)imino]acenaphthene) was reported.[96] Herein, the HT-phase (350 K) of 1:1 mixture of {$Yb^{III}(bian^{2-})$} and $Yb^{II}(bian^{\bullet-})$}, gradually transitions to a 3:1 mixture in the LT-phase (100 K). The presence of four crystallographically independent molecules in the unit cell, only one of which transitions, showcases, again, the sensitivity of the VT transition to minute structural differences.

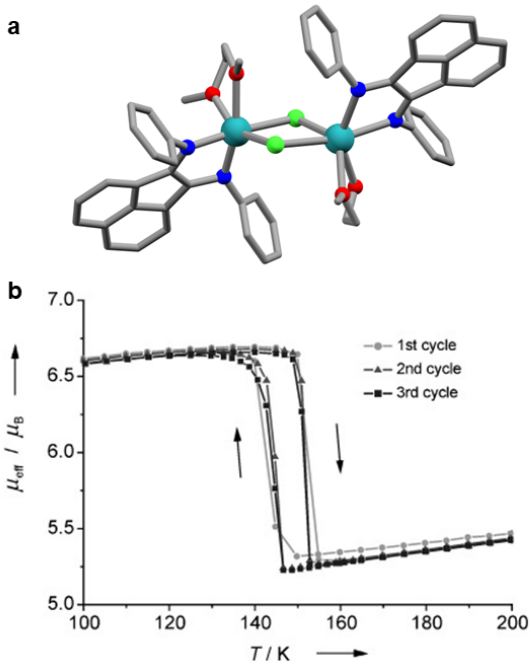

Fig. 3. (**a**) Molecular complex of [{(dpp-bian)Yb(dme)(μ-Cl) }$_2$].[95] Isopropyl groups and H-atoms are omitted for clarity. (**b**) Magnetic moment with temperature for several single-crystals of [{(dpp-bian)Yb(μ-Cl)(dme)}$_2$]. Reproduced with permission from ref. 95.

Changes in local coordination environment due to chemical pressure can also induce VT transitions in *Ln* molecular complexes. When functionalised *Ln*(Pc)$_2$ complexes, Ce{$(15C5)_4$Pc}$_2$[97] and Eu{$(BuO)_8$Pc}$_2$[98] are introduced into a Langmuir air/water monolayer, they undergo an electron transfer from one ligand to the metal, undergoing $Ce^{IV}\{Pc^{2-}\}_2$ ⇄ $Ce^{III}\{(Pc^{2-})(Pc^{\bullet-})\}$ and $Eu^{III}\{(Pc^{2-})(Pc^{\bullet-})\}$ ⇄ $Eu^{II}\{Pc^{\bullet-}\}_2$ transitions, respectively. For Ce{$(15C5)_4$Pc}$_2$, the surface pressure could be tuned to yield different tautomers. In Ce(Pc)$_2$, the same tautomerism could be induced by deposition on a gold surface, which induces a 45° twist between the $Pc^{2-/\bullet-}$ ligands, triggering the transition.[99]

Pairing *Ln* ions with other redox-active ligands such as cyclopentadienide or 2,2′-bpy ligands has led to the

observation of intermediate valency.[100] Here, close energetic proximity of ligand and *Ln* valence states lead to multi-configurational ground states, where the formal valence of both the *Ln* ion and ligand are non-integer. The Yb(Cp*)$_2$L systems, where L are derivatives of 2,2′-bpy, are particularly well studied examples of intermediate valence. Within this family, a phenomenon termed intermediate valence tautomerism (IVT) is exhibited by (Cp*)$_2$Yb(4,4′-Me$_2$-2,2′-bpy) (Fig. 4a).[101,102] In this compound, magnetometry and Yb L_3-edge X-ray absorption near-edge structure (XANES) spectra are consistent with a hysteretic valence transition between two distinct intermediate valence tautomers (Fig. 4b). These phenomena are now well established in both purely inorganic solids and molecular *Ln* complexes, whilst remaining elusive in coordination networks of any kind.

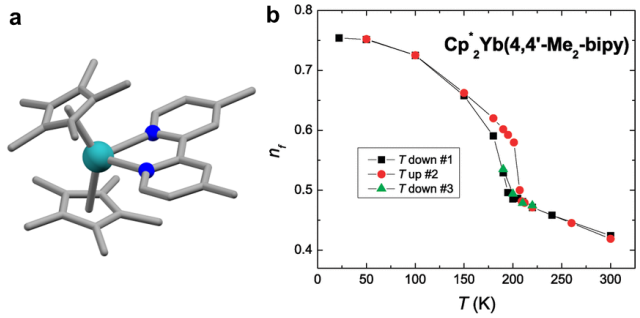

Fig. 4. (**a**) Structure of (Cp*)$_2$Yb(4,4′-Me$_2$-2,2′-bpy).[102] (**b**) *f*-hole occupancy (n_f) determined by fitting of XANES spectra across the thermal intermediate valence transition. Reprinted with permission from ref. 101. Copyright 2010 American Chemical Society.

5. Tiling valence, tautomerism & magnetism

5.1 Inspiration from transition metal tessellations

Coordination networks extending into one, two, or three dimensions, are the "missing link" between extended inorganic solids and molecular coordination complexes. This is well exemplified by the family of compounds spurred from the discovery of the 2D network CrCl$_2$(pyz)$_2$ (Fig. 5). The reducing nature of Cr^{II} leads to an electronic ground state approximated by the formulation Cr^{III}{(pyz^0)(pyz$^{\bullet-}$)}.[103] Strong metal-radical magnetic interactions and significant *π–d* conjugation lead to ferrimagnetic ordering at relatively high temperatures (55 K) and one of the highest observed electrical conductivities in a coordination compound.

Modulation of the Cr^{II}/Cr^{III} redox couple through ligand substitution of the *trans*-chlorido ligands for methanesulfonate yields instead Cr^{II}(pyz^0)$_2$, which is electrically insulating and exhibits an antiferromagnetic ground state.[104] A postsynthetic reduction of CrCl$_2$(pyz)$_2$ leads to formation of Li$_{0.7}$Cl$_{0.7}$Cr(pyz)$_2$·0.25 thf (thf = tetrahydrofuran), consisting of layers of Cr^{II}(pyz$^{\bullet-}$)$_2$. Here, the strong metal-radical interactions lead to a massive 0.75 T coercivity at room temperature, rivalling rare-earth based

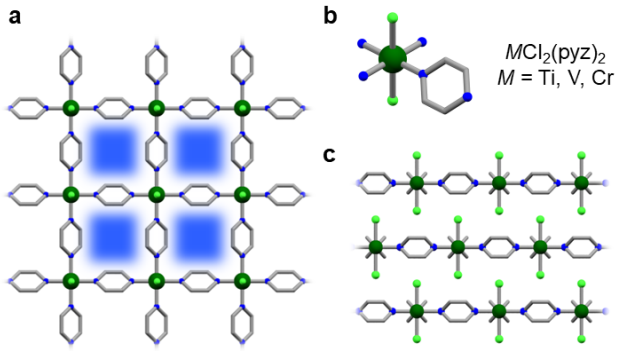

Fig. 5. (**a**) 2D square tilings formed by *M*Cl$_2$(pyz)$_2$. (**b**) Local coordination environment of *M* ions. (**c**) Packing of 2D sheets. Hydrogen atoms are omitted for clarity.[103]

hard magnets.[105] Similar layered 2D sheets to CrCl$_2$(pyz)$_2$ can be obtained with Ti and V.[106] TiCl$_2$(pyz)$_2$, approximated as Ti^{III}{(pyz^0)(pyz$^{\bullet-}$)}, displays strongly correlated Fermi liquid behaviour, leading to the highest room-temperature electronic conductivity for any metal-organic solid with octahedrally coordinated metal ions. In contrast, the antiferromagnetic insulator VCl$_2$(pyz)$_2$ exhibits no electron transfer from metal to ligand, leading to a V^{II}(pyz^0)$_2$ redox isomer. These highly correlated, extended materials are in stark contrast to the vast majority of typical framework materials, which are typically constructed from redox-inactive linkers and metal nodes.

5.2 Innocent Archimedean tessellations

Akin to the *M*Cl$_2$(pyz)$_2$ series, *trans*-dihalido *Ln* nodes could be similarly expected to structurally direct 2D sheet-like tessellations. Labile solvates of the *trans*-{*Ln*^{II}I$_2$} moieties are readily formed by dissolution of *Ln*I$_2$ forming what is posited to be *trans*-*Ln*I$_2$(CH$_3$CN)$_5$ (*Ln* = Sm, Eu, Yb)[107] in acetonitrile, and *trans*-*Ln*I$_2$(thf)$_5$ (*Ln* = Nd,[108] Sm,[109] Eu[110]) or *trans*-*Ln*I$_2$(thf)$_4$ (*Ln* = Yb[111]) in thf (Fig. 6). Unlike the *M*Cl$_2$(pyz)$_2$

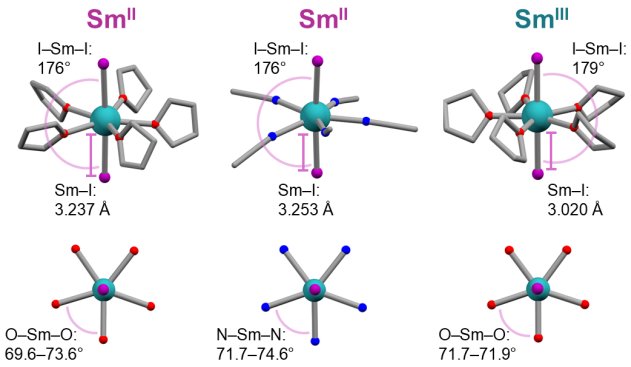

Fig. 6. Left to right: *Ln*^{II} precursors formed in solution: *Ln*I$_2$(thf)$_5$;[109] *Ln*I$_2$(CH$_3$CN)$_5$;[98] and a *Ln*^{III} solvate *Ln*I$_2$(thf)$_5^+$.[112] Selected angles shown indicate the *pseudo*-pentagonal bipyramidal coordination sphere. Sm–I bond lengths are highlighted to indicate the *ca*. 6% decrease in *Ln*–ligand bond lengths upon one-electron oxidation.

tessellations, where octahedral nodes lead to square tilings (Fig. 5), the {$Ln^{II}I_2$} nodes are *pseudo*-pentagonal bipyramidal, and as such should engender 2D tilings with five-fold nodes. The proof of principle was achieved through the combination of {$Yb^{II}I_2$} nodes with ditopic 4,4′-bipyridine (bpy), leading to either 2D sheets, $YbI_2(bpy)_{5/2}$, or *pseudo*-1D ladder structures, $YbI_2(bpy)_2(thf)$, depending on the reaction solvent (Fig. 7a, b).[113] In $YbI_2(bpy)_{5/2}$, irrespective of the close resemblance of the first coordination sphere of Yb to D_{5h} symmetry–incompatible with periodicity–the flexibility of the bpy ligands results in an elusive, idealized elongated triangular tessellation, consisting of triangular and quadratic motifs. Despite the large negative reduction potential of the Yb^{III}/Yb^{II} redox couple (Table 1), no full or partial electron transfer occurs between Yb^{II} and bpy, contrasting the observation in, e.g., $CrCl_2(pyz)_2$ ($E_{1/2}(Cr^{III}/Cr^{II})$ = –0.41 V). Confirmation of the Yb^{II} oxidation state in compounds $YbI_2(bpy)_{5/2}$ and $YbI_2(bpy)_2(thf)$ is reflected by their diamagnetism in the entire temperature range of 1.7–273 K. This assignment is further supported by bond length analysis, where the Yb–I bond length is a sensitive measure of the Yb oxidation state (Fig. 8).

A similar Archimedean tessellation, i.e., tiling of different polygons, to that of $YbI_2(bpy)_{5/2}$ has previously been observed by scanning tunnelling microscopy in on-surface self-assembled structures of Eu atoms and *para*-quaterphenyl–dicarbonitrile.[114] Herein, several metal-organic Archimedean tessellations were shown to form under near identical conditions suggesting little energetic difference. Notably, the random tessellation of triangles and squares led to the realization of a dodecagonal quasicrystalline phase. The observation of the periodic $YbI_2(bpy)_{5/2}$ quasicrystal approximant phase, suggests that similar 2D quasicrystalline materials could be designed in bulk, crystalline materials.[115,116] On a separate note, coordination networks incorporating divalent *Ln* ions instead of the much more common trivalent ions are rare.[117,118,119] The spontaneous self-assembly of $YbI_2(bpy)_{5/2}$ and $YbI_2(bpy)_2(thf)$ suggests that a wealth of, in coordination chemistry, hitherto unknown tessellations may be readily obtainable.

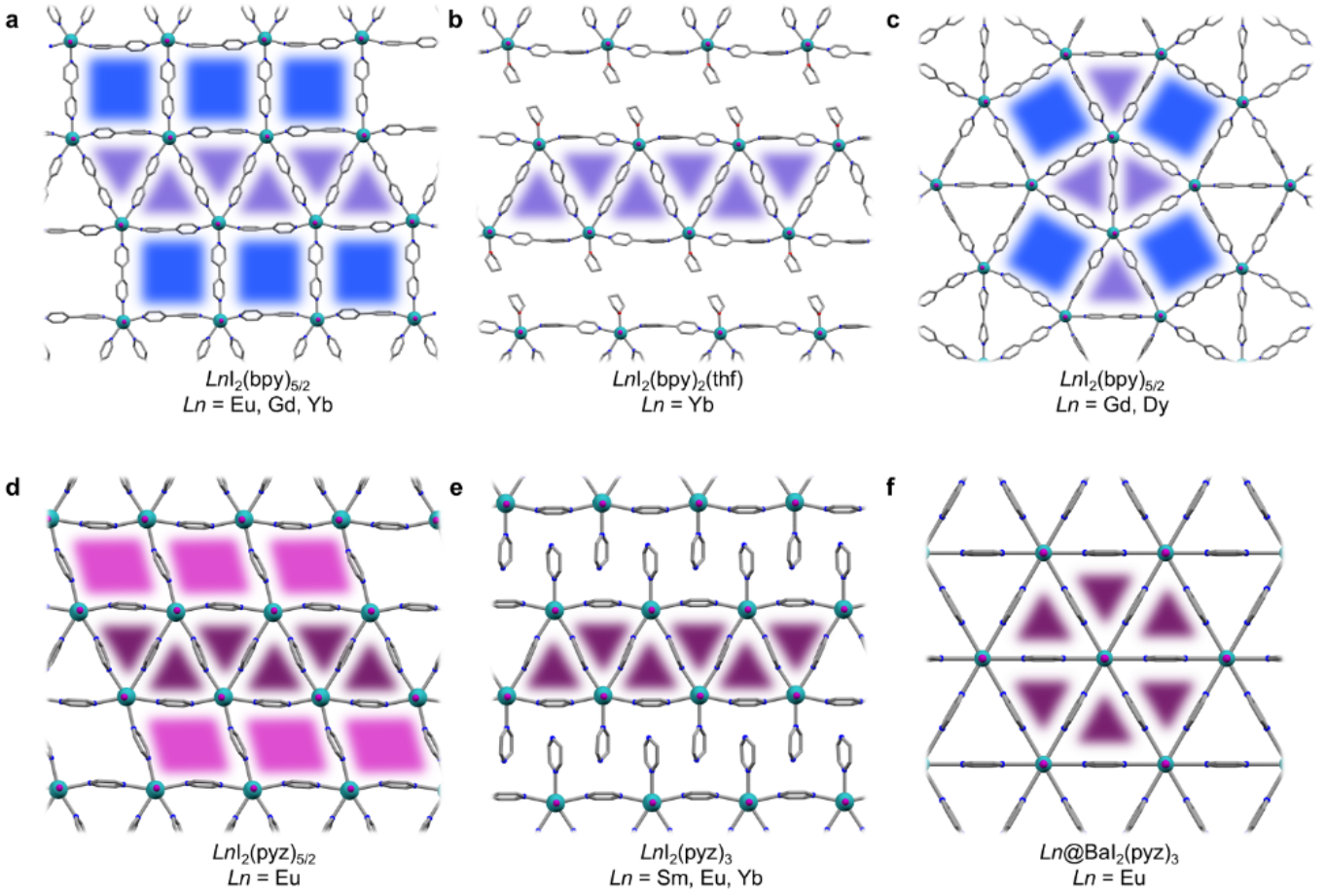

Fig. 7. Representation of 2D tessellations formed through the combination of *trans*-{LnI_2} nodes with ditopic pyz and bpy ligands. (**a**) Elongated triangular net $LnI_2(bpy)_{5/2}$.[113,120,121] (**b**) *Pseudo*-1D chains of $LnI_2(bpy)_2(thf)$.[113] (**c**) Snub square net $LnI_2(bpy)_{5/2}$.[120] (**d**) Elongated triangular net $LnI_2(pyz)_{5/2}$.[121] (**e**) *Pseudo*-1D chains of $LnI_2(pyz)_3$.[125] (**f**) Triangular net of $Ln@BaI_2(pyz)_3$.[124]

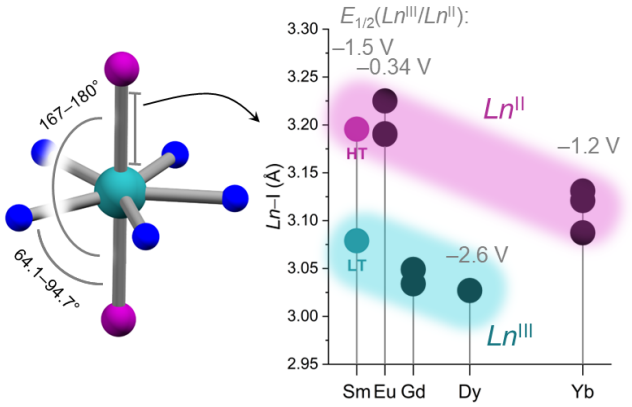

Fig. 8. Local coordination sphere of $LnI_2(bpy)_x$, $LnI_2(pyz)_x$ (left), highlighting typical bond angles. Plot of *Ln*–I bond lengths across the *Ln* series (right), with groups of Ln^{II} and Ln^{III} oxidation states highlighted. For $SmI_2(pyz)_3$, a HT and LT tautomer can be identified.

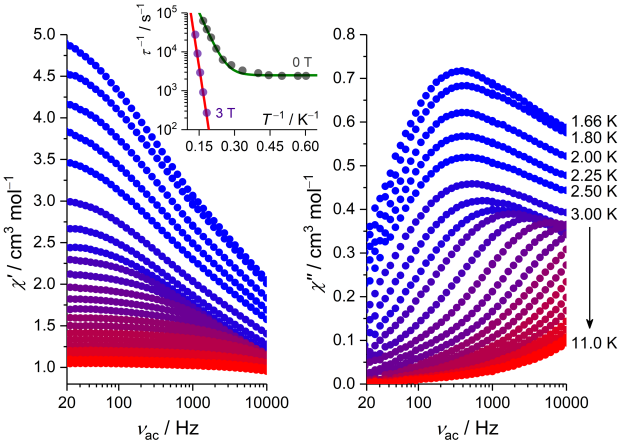

Fig. 9. In-phase (χ', left) and out-of-phase (χ'', right) ac susceptibility data for polycrystalline $DyI_2(pyz)_{5/2}$ obtained at selected temperatures and in the absence of a static (dc) magnetic field. Inset: temperature dependence of the paramagnetic relaxation rate, τ^{-1}, vs temperature. The solid lines are simulations, yielding an effective energy barrier to magnetization reversal of 63 cm^{-1} when measured in H_{dc} = 3 T. Reprinted with permission from ref. 120. Copyright 2021 American Chemical Society.

5.3 Guilty magnetic tilings

In order to leverage the magnetic properties of *Ln*-based materials, paramagnetic *Ln* ions were sought. Further, inspired by the burgeoning literature on *Ln*-radical complexes and their extraordinary magnetic properties, actuation of ligand scaffold non-innocence was pursued. Compared to the less reducing Yb^{II}, the largely negative reduction potential of, e.g., Dy^{II} (Table 1) is such that even many common solvents are reduced, making exotic reagents like DyI_2 impractical. Instead of relying on an *in situ* reduction of the ligand by the Ln^{II} ion, the solution reaction of trivalent LnI_3 (*Ln* = Gd, Dy) with a mixture of bpy^0 and $bpy^{\bullet-}$, formed simply by Na reduction, yields 2D networks of formula $LnI_2(bpy)_{5/2}$, analogous to the previously discussed $YbI_2(bpy)_{5/2}$.[120] However, for *Ln* = Gd, Dy, a snub square tiling structure is obtained (Fig. 7c), as well as a side-phase of the elongated triangular tiling for Gd (Fig. 7a). For both $DyI_2(bpy)_{5/2}$ and $GdI_2(bpy)_{5/2}$, the *Ln*–I bond length analyses are consistent with the presence of Ln^{III} ions (Fig. 8), implying a radical nature of the bpy scaffold and an approximate electronic configuration of $Ln^{III}\{(bpy^{\bullet-})(bpy^0)_{3/2}\}$. The ligand scaffold mixed-valency is reminiscent of the situation encountered in $CrCl_2(pyz)_2$, however, the absence of any intervalence charge transfer transitions in $GdI_2(bpy)_{5/2}$ suggests weakly electronically coupled bpy fragments and an anticipated poor electrical conductivity.

The magnetometric data for $GdI_2(bpy)_{5/2}$ suggest only weak antiferromagnetic Gd^{III}–$bpy^{\bullet-}$ exchange interactions, on the order of J = –0.73 cm^{-1} ($-2J\,\hat{S}_1\hat{S}_2$ convention), as often encountered in *Ln*–radical systems. This number, however, is significantly smaller than those found in the previous discussed molecular complexes.[68-72] In the case of $DyI_2(bpy)_{5/2}$, the axial ligand field induced by the anionic *trans*-iodido ligands combined with a *pseudo*-D_{5d} symmetry at the Dy^{III} centre allows for the observation of slow paramagnetic relaxation in zero applied magnetic field (Fig. 9). However, despite the presence of a small Dy^{III}–$bpy^{\bullet-}$ exchange bias, rapid quantum tunnelling of magnetisation is observed.

The isolation of a snub square tiling in a coordination network is exceedingly rare, with only one prior example known in the bulk phase.[116] The coexistence of both the elongated triangular and snub square tessellation in the case of $GdI_2(bpy)_{5/2}$ may suggest similar energies of formation and, thus, provide perspectives for the isolation of intergrown motifs required for quasicrystallinity.

5.3 Frosty frustrated triangles

The formation of Archimedean tessellations is a robust outcome of the assembly of $\{LnI_2\}^{0/+}$ units with also different ditopic ligands. This is illustrated by the isoreticular $EuI_2(bpy)_{5/2}$ and $EuI_2(pyz)_{5/2}$, both forming the elongated triangular tessellation (Fig. 7a, d).[121] Switching the long bpy ligand for shorter pyz leads to essentially identical coordination at the Eu centre, although modulates the Eu···Eu distances, and thus directly impacts the magnetic interaction strengths. The only weakly reducing nature of Eu^{II} inhibits any radical character of the ligand scaffold, as confirmed by bond length analysis (Fig. 8), magnetometry and X-ray absorption spectroscopy. The $4f^7$ electronic configuration of Eu^{II} leads to the largest possible spin magnetic moment and the absence of an orbital angular momentum results in a vanishingly small magnetic anisotropy. These qualities are tantalizing for the development of Eu^{II}-based coolant materials for adiabatic demagnetization refrigerators relying on the magnetocaloric effect (MCE).[122,123] The MCE occurs due to the change in magnetic entropy of a material when a magnetic field is applied or removed. When the field is applied, the constituent spins of the magnet align, reducing magnetic entropy, and the system releases heat. When the field is removed, entropy increases as the spin moments randomize, absorbing heat and cooling the material. MCE materials operating in the sub-Kelvin regime are touted as alternatives to traditional ^{3}He cooling used, e.g., for

cryogenic applications needed in quantum technology and space exploration. In this temperature window, even weak antiferromagnetic interactions are undesired, as they minimize the ground state spin moment and thus the magnetic entropy. Nevertheless, complete eradication of magnetic interactions between electronic spins is only possible in magnetically highly dilute materials, which concurrently will have an only low cooling capacity. The creation of ideal triangular motifs bypasses this obstacle. In an equilateral triangle it is impossible to satisfy only pairwise antiferromagnetic interactions, leading to magnetic frustration, absence of long-range magnetic order, and a retention of the magnetic entropy extending into the sub-Kelvin domain. Indeed, $EuI_2(pyz)_{5/2}$ fulfills these requirements by featuring triangular motifs with weak antiferromagnetic interactions, on the order of –0.3 cm^{-1}, as suggested by DFT calculations. The specific heat shows a broad maximum in the zero-field c_p between *ca*. 0.7 and 3 K, attributed to 2D intra-layer fluctuations. However, below 0.5 K, there is the onset of a magnetic phase transition, negating the observation of a magnetocaloric effect below this temperature. Despite this, a sizeable MCE is observed with a maximum isothermal magnetic entropy change of 24.3 J kg^{-1} K^{-1} for a 7 T field change and at a high temperature of 3 K. To further improve the MCE at sub-K temperature in Eu^{II} tessellations, we sought to realize strictly triangular motifs. This situation is fulfilled in the triangular tessellation, featuring 3- or 6-fold symmetric nodes, yet to be observed in a coordination solid. As the ionic radius of Eu^{II} is slightly too small to accommodate the required 6 ligands in plane, the larger Ba^{II}, was used. This resultant compound, $BaI_2(pyz)_3$ (Fig. 7f), features sheets with a triangular tessellation, with crystallographic D_{3d} local symmetry.[124] Despite the nonexistence of the Eu^{II} analogue, performing the synthesis with a mixture of EuI_2 and BaI_2 leads to alloyed networks, $Ba_{1-x}Eu_xI_2(pyz)_3$, with up to 92% of Eu^{II} (hereafter denoted as $Ba_{0.1}Eu_{0.9}I_2(pyz)_3$). In the absence (or less than 8%) of templating Ba^{II}, $EuI_2(pyz)_3$ is instead formed. Here, a different connectivity is observed, with the smaller Eu^{II} nodes enjoying a fivefold in-plane coordination (Fig. 7e). Structural analysis of $Ba_{0.1}Eu_{0.9}I_2(pyz)_3$, is consistent with a Eu^{II} oxidation state, and reveals the longest reported unsupported Eu–N bond lengths (2.90 Å). The resultant long Eu···Eu distances lead to exceedingly weak exchange interactions, which is reflected by the weak antiferromagnetic J = −0.006 cm^{-1} obtained from the concerted analysis of magnetometric and heat capacity data obtained down to 0.3 K (Fig. 10a). The ensuing magnetic frustration tied to the interactions and the high crystallographic symmetry leads to a magnetocaloric working temperature as low as T = 0.17 K (Fig. 10b). This value is remarkably low for a relatively magnetically dense refrigerant and illustrates well how coordination chemistry approaches towards novel MCE materials may challenge the much more established purely inorganic materials.

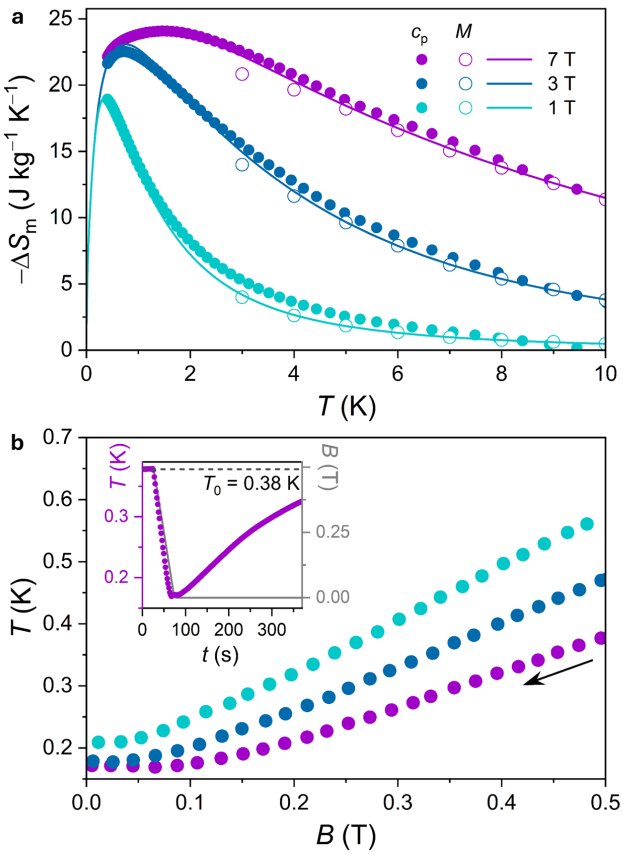

Fig. 10. The change in magnetic entropy, $-\Delta S_m$, at selected magnetic fields for $Ba_{0.1}Eu_{0.9}I_2(pyz)_3$, as obtained from the experimental c_p and magnetization data, and calculated c_p for J/k_B = −0.008 K and D/k_B = 0.068 K (lines). b) Demagnetization (0.5 T → 0 T) processes at starting temperatures T_0 = 0.58, 0.47 K, and 0.38 K. Inset: time-dependence of the temperature at T_0 = 0.38 K following a linear decrease in the magnetic field strength (grey trace). Reproduced from ref.124.

5.4 Emergence of lanthanide valence swings

As for $EuI_2(pyz)_3$, the combination of LnI_2 (Ln = Sm, Yb) with pyz leads to the formation of $LnI_2(pyz)_3$ (Fig. 7e), featuring *pseudo*-1D chains of $\{LnI_2pyz_2\}$ with interdigitating pendant pyz ligands.[125] All data for both $EuI_2(pyz)_3$ and $YbI_2(pyz)_3$ are consistent with the presence of a Ln^{II} ion. For Sm^{II}, despite the diamagnetic $^7F_0$ ground state, thermal population of the $^7F_1$ state gives rise to a sizable magnetic moment at room temperature ($\chi T \approx 1.4$ cm^3 mol^{-1} K^{-1}), as found in, e.g., $Sm^{II}I_2(CH_3CN)_5$.[107] For $SmI_2(pyz)_3$, the room-temperature χT product is commensurate with an Sm^{II} oxidation state assignment. Upon descending temperature, an abrupt decrease in χT of ~80% is observed at $T \approx 190$ K. Sm–I bond length analysis of the single-crystal X-ray structures of the HT and LT phases suggests the presence of a $Sm^{II}(pyz^0)_3$ HT tautomer and a $Sm^{III}\{(pyz^0)_2(pyz^{\bullet-})\}$ LT tautomer (Fig.s 8, 11a). As expected for an $Sm^{II} \rightarrow Sm^{III}$ oxidation, a 4% decrease in Ln–I bond lengths is observed and an overall 6% reduction in the unit cell volume. The structural analysis of the LT phase clearly shows the localization of the $pyz^{\bullet-}$ moieties in a zigzag chain between the Sm^{III} ions (Fig. 11a). Additional evidence of a VT transition is provided by XANES of the HT and LT phases (Fig. 11c). The Sm L_3 absorption edge resonance shows a shift of 8 eV, consistent with a quantitative and

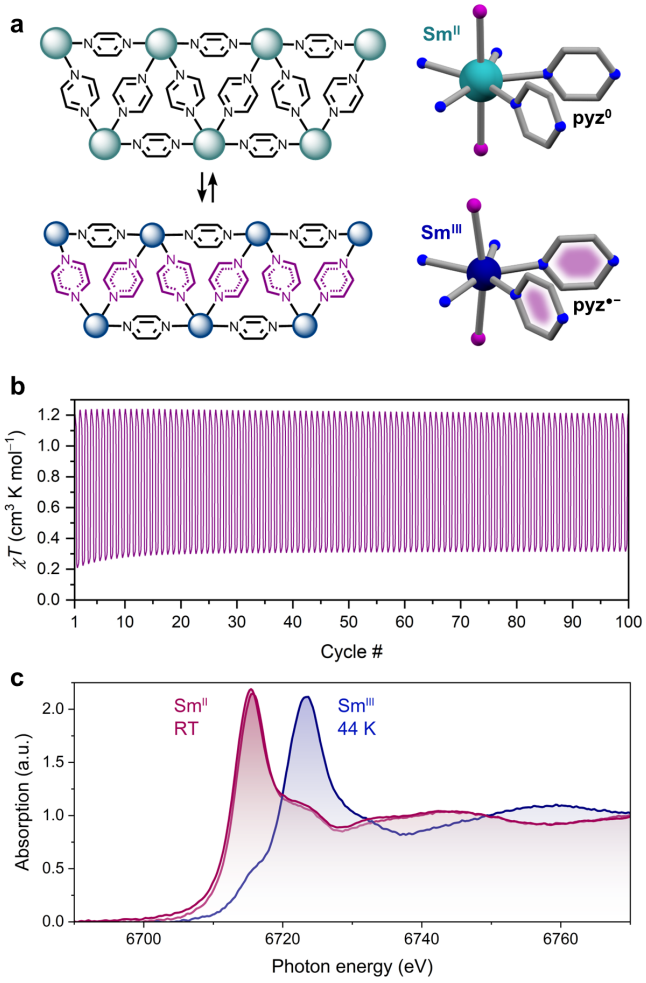

Fig. 11. (**a**) HT and LT tautomers of the *pseudo*-1D chains of {Sm(pyz)$_2$} in SmI$_2$(pyz)$_3$. Local coordination environment of the Sm ions shown on the right. (**b**) Durability of the VT transition as reflected in the χT data obtained by T cycling between 175 K and 225 K (sweep rate = 2 K min^{-1}). (**c**) Samarium L_3 XANES spectra of polycrystalline SmI$_2$(pyz)$_3$ measured at 300 K, at 44 K and again at 300 K. Reproduced from ref. 125.

reversible Sm^{II}(pyz^0)$_3$ ⇄ Sm^{III}{(pyz^0)$_2$(pyz$^{\bullet-}$)} VT transition, and no indication of intermediate valency. The VT transition is cooperative and has an open thermal hysteresis of 14 K (sweep rate = 0.5 K min^{-1}) and is reversible over at least 100 temperature cycles with only minor loss of conversion (Fig. 11b). The electronic ground state of Sm^{III}, $^6H_{5/2}$ with g_J = 2/7, results in an almost vanishing magnetic moment. As such, the magnetic moment of the LT phase is dominated by the magnetic moment of pyz$^{\bullet-}$. The close proximity of the pyz$^{\bullet-}$ in the zigzag chain results in strong radical–radical magnetic exchange interactions (J = −76 cm^{-1}). The isomorphism of the *Ln*I$_2$(pyz)$_3$ (*Ln* = Sm, Eu, Yb) series provides the opportunity to tune the VT transition by alloying, as often used in inorganic solids exhibiting VT transitions. Indeed, syntheses involving mixtures of SmI$_2$ and YbI$_2$ in any ratio yield monophasic Sm$_{1-x}$Yb$_x$I$_2$(pyz)$_3$ solid-solutions. The smaller ionic radius of Yb^{II} over Sm^{II}, results in a progressive reduction in the HT unit cell volume with increasing Yb content. Introducing only 10% Yb^{II} yields an alloy retaining full a full VT transition, but at a lower critical temperature (Fig. 12). A further increase in Yb content leads to a further shifting of the VT critical temperature, a softening of the VT transition, and a narrowing of the thermal hysteresis, consistent with decreasing cooperativity. Notably, this is fully analogous to both the situation encountered in SCO coordination polymers, as well as the established *Ln* VT transitions in purely inorganic materials. In stark contrast to the purely inorganic solids, however, the VT transition in SmI$_2$(pyz)$_3$ and Sm$_{1-x}$Yb$_x$I$_2$(pyz)$_3$ appears to involve only distinct and integer oxidation state, and in this regard bear closer resemblance to the VT transitions observed in transition metal-based systems.

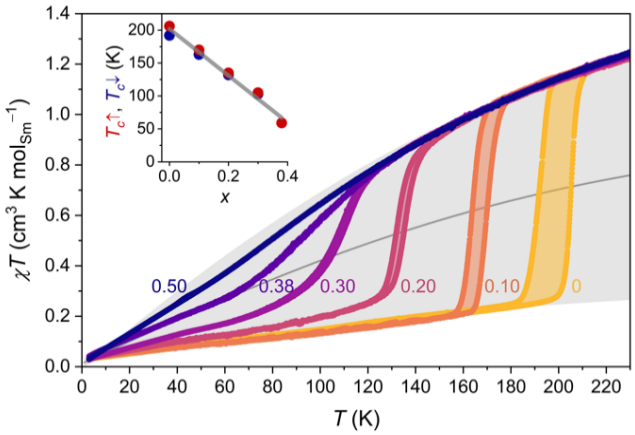

Fig. 12. Magnetic susceptibility–temperature product, χT ($\mu_0 H$ = 1.0 T; temperature ramping rate, 0.25 K min^{-1}) of Sm$_{1-x}$Yb$_x$I$_2$(pyz)$_3$ solid solutions, normalized to the samarium content, 1 − x. The grey surface represents the area spanned by the expected χT product for the LT phase and HT phase. The solid black line represents the 50% molar fraction of the LT ⇄ HT phase conversion. Inset: temperature dependence of T_c versus x, with the best linear fit (grey line, T_c (K) = −3.55x + 202). Reproduced from ref. 125.

6. Conclusions and outlook

The self-assembly of *trans*-{*Ln*I$_2$}$^{0/+}$ nodes and ditopic linkers, pyrazine and 4,4′-bipyridine, yields a variety of genuinely new chemical motifs. The robust structure-directing nature of the nodes provide rare opportunities for tailoring symmetries in *f*-element-based materials. The 2D tessellations escape the periodicity-defying pentagonal nodes by tiling Archimedean patterns, that may verge on even quasicrystallinity. Harnessing a novel templation effect, even hexagonal nodes can be realized. The structural symmetry has decisive implications for the electronic structure and ensuing physical properties. This is exemplified by the spin-frustrated Ba$_{0.1}$Eu$_{0.9}$I$_2$(pyz)$_3$ network, which escapes magnetic order, even when approaching absolute zero. The wide span of *Ln*^{III}/*Ln*^{II} reduction potentials and the chemical resemblance allows for the design of isostructural materials hosting either *Ln*^{II}–ligand(0) or *Ln*^{III}–ligand(•–) linkages. Despite being well-established in purely inorganic materials, stimuli-induced VT transitions linking the *Ln*^{II}–ligand(0) or *Ln*^{III}–ligand(•–) states are far from well-established. Sm^{II} and pyrazine are on the brink of electron

transfer. The resultant compound, $SmI_2(pyz)_3$, is the first molecule-based material of the *f*-block to exhibit an unambiguous and complete VT transition. The phenomenon is robust to structural distortions, although tunable, as illustrated by molecular alloying. The realization of a VT switch in a coordination network opens perspectives for further chemically encoding of cooperative VT events by crystal engineering, as successfully pursued in the field of SCO materials. However, the fundamental advantage to coordination networks featuring VT transitions is the concerted change to the extended electronic structure of the pillaring ligands. Such activation of the otherwise innocent scaffold is currently at the origin of new horizons of metal-organic framework chemistry, such as high electrical conductivity.[126,127] We envision a plethora of magnetoelectrical properties, not currently found in molecular chemistry, could be found in the chemical space of valence-fluctuating lanthanide ions and redox-non-innocent scaffolds.

K.S.P. thanks the VILLUM Foundation for a VILLUM Young Investigator+ (42094) grant, the Independent Research Fund Denmark for a DFF-Sapere Aude Starting grant (no. 0165-00073B), and the Carlsberg Foundation for a research infrastructure grant (no. CF17-0637).

Author Contributions

The manuscript was written by K.S.P. and M.A.D., and both authors have given their consent to the publication of the manuscript.

Conflicts of interest

There are no conflicts to declare.

References

1 O. Sato, *Nat. Chem.*, 2016, **8**(*7*), 644-656.
2 M. A. Halcrow, *Chem. Soc. Rev.*, 2011, **40**(*7*), 4119-4142.
3 T. Tezgerevska, K. G. Alley, C. Boskovic, *Coord. Chem. Rev.*, 2014, **268**, 23-40.
4 G. K. Gransbury, C. Boskovic, Encyclopedia of Inorganic and Bioinorganic Chemistry, John Wiley & Sons Ltd., New Jersey, USA 2021, 1–24.
5 A. S. Attia, C. G. Pierpont, *Inorg. Chem.*, 1995, **34**, 1172-1179.
6 A. A Kamin, I. P. Moseley, J. Oh, E. J. Brannan, P. M. Gannon, W. Kaminsky, J. M. Zadrozny, D. J. Xiao, *Chem. Sci.*, 2023, **14**, 4083-4090.
7 L.-T. Yue, S. O. Shapovalova, J.-S. Hu, M. G. Chegerev, Y.-M. Zhao, C.-D. Liu, M. Yu, A. A. Starikova, A. A. Guda, Z.-S. Yao, J. Tao, *Angew. Chem. Int. Ed.* 2024, **63**, e202401950.
8 Y.-M. Zhao, J. P Wang, X. Y.Chen, M. Yu, A. A.Starikova, J. Tao, *Inorg. Chem. Front.*, 2023, **10**, 7251-7264.
9 K. KC, T. Woods, L. Olshansky, *Angew. Chem. Int. Ed.* 2023, **62**, e202311790.
10 S. Wiesner, A. Wagner, E. Kaifer, H.-J. Himmel, *Chem. Eur. J.* **2016**, *22*, 10438-10445.
11 L. Greb, *Eur. J. Inorg. Chem.* 2022, e202100871.
12 J. Bendix, K. M Clark, *Angew. Chem. Int. Ed*. 2016, **55**, 2748–2752.
13 R. M. Buchanan, C. G. Pierpont, *J. Am. Chem. Soc*. 1980, **102**(*15*), 4951–4957.
14 O. Sato, A. Cui, R. Matsuda, J. Tao, S. Hayami, *Acc. Chem. Res.*, 2007, **40**(*5*), 361-369.
15 L. Leroy, T. M. Francisco, H. J. Shepherd, M. R. Warren, L. K. Saunders, D. A. Shultz, P. R. Raithby, and C. B. Pinheiro, *Inorg. Chem.* 2021 **60** , 8665-8671.
16 W. H. Xu, Y. B. Huang, W.-W. Zheng, S. Q. Su, S. Kanegawa, S. Q. Wu, O. Sato, *Dalton Trans*., 2024, **53**, 2512-2516.
17 A. Summers, F. Z. M. Zahir, G. F. Turner, M. A. Hay, A. Riboldi-Tunnicliffe, R. Williamson, S. Bird, L. Goerigk, C. Boskovic, S. A. Moggach, *Nat. Commun.,* 2024, **15**, 8922.
18 C. Roux, D. M. Adams, J. P. Itié, A. Polian, D. N. Hendrickson, M. Verdaguer, *Inorg. Chem.* 1996, **35**, 2846–2852.
19 G. Poneti, M. Mannini, L. Sorace, P. Sainctavit, M. A. Arrio, E. Otero, J. Criginski Cezar, A. Dei, *Angew. Chem.* 2010, **122**, 1998 –2001.
20 G. Poneti, L. Poggini, M. Mannini, B. Cortigiani, L. Sorace, E. Otero, P. Sainctavit, A. Magnani, R. Sessoli and A. Dei, *Chem. Sci.,* 2015, **6**, 2268-2274.
21 S. Bin-Salamon, S. Brewer, S. Franzen, D. L. Feldheim, S. Lappi, D. A. Shultz, *J. Am. Chem. Soc.*, 2005, **127**, 5328–5329.
22 O Kahn, J Kröber, C Jay, *Adv. Mater.*, 1992, **4**, 718-728.
23 J. Krober, E. Codjovi, O. Kahn, F. Groliere, C. Jay, *J. Am. Chem. Soc.* 1993, **115**, 9810–9811.
24 J. Cruddas, B. J. Powell, *Inorg. Chem. Front.*, 2020, **7**, 4424-4437.
25 M. Ahmed, K. A. Zenere, N. F. Sciortino, K. S. A. Arachchige, G. F. Turner, J. Cruddas, C. Hua, J. R. Price, J. K. Clegg, F. J. Valverde-Muñoz, J. A. Real, G. Chastanet, S. A. Moggach, C. J. Kepert, B. J. Powell, S. M. Neville, *Inorg. Chem.*, 2022, **61**, 6641-6649.
26 A. Günther, Y. Deja, M. Kilic, K. Tran, P. Kotra, F. Renz, W. Kowalsky, B. Roth, *Sci. Rep.*, 2024 **14**, 5897.
27 C. H. Pham and F. Paesani, *Inorg. Chem*. 2018, **57**, 9839–9843.
28 P. D. Southon, L. Liu, E. A. Fellows, D. J. Price, G. J. Halder, K. W. Chapman, B. Moubaraki, K. S. Murray, J.-F. Létard, C. J. Kepert, *J. Am. Chem. Soc.*, 2009, **131**(*31*), 10998–11009.
29 B. Li, L.-Q. Chen, R.-J. Wei, J. Tao, R.-B. Huang, L.-S. Zheng, Z. Zheng, *Inorg. Chem.*, 2011, **50**, 424–426.
30 O. Drath, R. W. Gable, B. Moubaraki, K. S. Murray, G. Poneti, L. Sorace, C. Boskovic, *Inorg. Chem.*, **55**, 4141-4151.
31 O. Drath, C. Boskovic, *Coord. Chem. Rev.*, 2018, **375**, 256-266.
32 B. Li, Y.-M. Zhao, A. Kirchon, J.-D. Pang, X.-Y. Yang, G.-L. Zhuang, H.-C. Zhou, *J. Am. Chem. Soc.*, **141**, 6822-6826.
33 A. Lannes, Y. Suffren, J. B. Tommasino, R. Chiriac, F. Toche, L. Khrouz, F. Molton, C. Duboc, I. Kieffer, J.-L. Hazemann, C. Reber, A. Hauser, D. Luneau, *J. Am. Chem. Soc.*, 2016, **138**, 16493-16501.
34 E. Evangelio, D. Ruiz-Molina, *C. R. Chimie*, 2008, **11**, 1137-1154.
35 G. K. Gransbury, M.-E. Boulon, S. Petrie, R. W. Gable, R. J. Mulder, L. Sorace, R.Stranger, C. Boskovic, *Inorg. Chem.*, 2019, **58**, 4230–4243.
36 F. Z. M. Zahir, M. A. Hay, J. T. Janetzki, R. W. Gable, L. Goerigk, C. Boskovic, *Chem. Sci.*, 2024, **15**, 5694-5710.
37 D. J. R. Brook, J. DaRos, A. Ponnekanti, S. Agrestini, E. Pellegrin, *Dalton Trans*., 2024, **53**, 7536-7545.

38 J. M. D Coey, *Engineering*, 2020, **6**, 119-131.
39 C. A. P. Goodwin, F. Ortu, D. Reta, N. F. Chilton, D. P. Mills, *Nature*, 2017, **548**, 439–442.
40 F.-S. Guo, B. M. Day, Y.-C. Chen, M.-L. Tong, A. Mansikkamäki, R. A. Layfield, *Science*, 2018, **362**, 1400-1403.
41 C. A. Gould, K. R. McClain, D. Reta, J. G. C. Kragskow, D. A. Marchiori, E. Lachman, E.-S. Choi, J. G. Analytis, R. D. Britt, N. F. Chilton, B. G. Harvey, J. R. Long, *Science*, 2022, **375**, 198-202.
42 A. Fatima, M. W. Ahmad, A. K. A. Al Saidi, A. Choudhury, Y. Chang, G. H. Lee, *Nanomaterials*, **11**, 2449.
43 A. V. Pavlishchuk, V. V. Pavlishchuk, *Theor. Exp. Chem.*, 2020, **56**, 1-25.
44 J. C. G. Bünzli, *Eur. J. Inorg. Chem.*, 2017, **44**, 5058-5063.
45 M. E. Fieser, M. R. MacDonald, B. T. Krull, J. E. Bates, J. W. Ziller, F. Furche, W. J. Evans, *J. Am. Chem. Soc.*, 2015, **137**(*1*), 369–382.
46 M. R. MacDonald, J. E. Bates, J. W. Ziller, F.Furche, W. J. Evans, *J. Am. Chem. Soc.* 2013, **135**, 9857–9868.
47 K. R. Meihaus, M. E. Fieser, J. F. Corbey, W. J. Evans, J. R. Long, *J. Am. Chem. Soc*., 2015, **137**(31), 9855–9860.
48 M. R. MacDonald, J. E. Bates, M. E. Fieser, J. W. Ziller, F. Furche, W. J. Evans, *J. Am. Chem. Soc.*, 2012, **134**, 8420–8423.
49 N. T. Rice, I. A. Popov, D. R. Russo, T. P. Gompa, A. Ramanathan, J. Bacsa, E. R. Batista, P. Yang, H. S. La Pierre, *Chem. Sci.*, 2020, **11**, 6149-6159.
50 H. Tateyama, A. C. Boggiano, C. Liao, K. S. Otte, X. Li, H. S. La Pierre, *J. Am. Chem. Soc.*, 2024, **146**(*15*), 10268-10273.
51 Y. Qiao, H. Yin, L. M. Moreau, R. Feng, R. F. Higgins, B. C. Manor, P. J. Carroll, C. H. Booth, J. Autschbach, E. J. Schelter, *Chem. Sci.*, 2021, **12**(*10*), 3558-3567.
52 A. Ramanathan, J. Kaplan, D. C. Sergentu, J. A. Branson, M. Ozerov, A. I. Kolesnikov, S. G. Minasian, J. Autschbach, J. W. Freeland, Z. Jiang, M. Mourigal, H. S. La Pierre, *Nat. Commun.*, 2023, **14**, 3134.
53 A. R. Willauer, C. T. Palumbo, F. Fadaei-Tirani, I. Zivkovic, I. Douair, L. Maron, M. Mazzanti, *J. Am. Chem. Soc.*, 2020, **142**, 5538-5542.
54 N. T. Rice, I. A. Popov, D. R. Russo, J. Bacsa, E. R. Batista, P. Yang, P., J. Telser, H. S. La Pierre, *J. Am. Chem. Soc.*, 2019, **141**, 13222-13233.
55 A. R. Willauer, I. Douair, A. S. Chauvin, F. Fadaei-Tirani, J. C. G. Bünzli, L. Maron, M. Mazzanti, *Chem. Sci.*, 2022, **13**, 681-691.
56 T. P. Gompa, A. Ramanathan, N. T. Rice, H. S. La Pierre, *Dalton Trans.*, 2020, **49**, 15945-15987.
57 M. A. Hay, C. Boskovic, *Chem. - Eur. J.*, 2021, **27**, 3608-3637.
58 L. R. Morss, *Chem. Rev.* 1976, 76, 827–841
59 M. Suta, C. Wickleder, *J. Lumin.*, 2019, **210**, 210-238.
60 C. A. Gould, K. R. McClain, J. M. Yu, T. J. Groshens, F. Furche, B. G. Harvey, J. R. Long, *J. Am. Chem. Soc.*, 2019, **141**, 12967– 12973
61 M. Szostak, D. J. Procter, *Angew. Chem. Int. Ed.*, 2012, **51**, 9238-9256.
62 T. C. Jenks, M. D. Bailey, J. L. Hovey, S. Fernando, G. Basnayake, M. E. Cross, W. Lia, M. J. Allen, *Chem. Sci.*, 2018, **9**, 1273-1278.
63 E. A. Boyd, C. Shin, D. J. Charboneau, J. C. Peters, S. E. Reisman, *Science*, 2024, **385**, 847-853.
64 K. C. Nicolaou; S. P. Ellery; J. S. Chen, *Angew. Chem. Int. Ed.*, 2009, **48**, 7140–7165.
65 K. Gopalaiah, H. B. Kagan, *Chem. Rec.*, 2013, **13**, 187-208.
66 S. Demir, I. R. Jeon, J. R. Long, T. D. Harris, *Coord. Chem. Rev.*, 2015, **289**, 149-176.
67 N. Ishikawa, M. Sugita, T. Ishikawa, S.-Y. Koshihara, Y. Kaizu, *J. Am. Chem. Soc.*, 2003, **125**, 8694-8695.
68 J. D. Rinehart, M. Fang, W. J. Evans, J. R. Long, *Nat. Chem.* 2011, **3**, 538–542.
69 J. D. Rinehart, M. Fang, W. J. Evans, J. R. Long, *J. Am. Chem. Soc.*, 2011, **133**, 14236-14239.
70 S. Demir, M. I. Gonzalez, L. E. Darago, W. J. Evans, J. R. Long, *Nat. Commun.*, 2017, **8**, 2144.
71 N. Mavragani, D. Errulat, D. A. Gálico, A. A. Kitos, A. Mansikkamäki, M. Murugesu, *Angew. Chem. Int. Ed.*, 2021, **60**, 24206 – 24213.
72 N. Bajaj, N. Mavragani, A. A. Kitos, D. Chartrand, T. Maris, T., A. Mansikkamäki, M. Murugesu, *Chem*. **10**, 2484-2499.
73 S. N. Gilbert Corder, X. Chen, S. Zhang, F. Hu, J.i Zhang, Y. Luan, J. A. Logan, T. Ciavatti, H. A. Bechtel, M. C. Martin, M. Aronson, H. S. Suzuki, S.-I. Kimura, T. Iizuka, Z. Fei, K. Imura, N. K. Sato, T. H. Tao, M. Liu, *Nat. Commun.*, 2017, **8**, 2262.
74 M. Owen, *Ann. Phys.*, 1912, **37** 657-699.
75 A. W. Lawson, T.-Y. Tang, *Phys. Rev.*, 1949, **76**, 301.
76 K.A. Gschneidner Jr., R. Smoluchowski, *J. Less Common Met.* 1963, **5**, 374-385.
77 A. Sousanis, P. F. Smet, D. Poelman, *Materials*, 2017, **10**, 953.
78 J. M. Lawrence, R. D. Parks, *J. Phys. Colloques*, 1976, **37**, C4-249.
79 A. Jayaraman, V. Narayanamurti, E. Bucher, and R. G. Maines, *Phys. Rev. Lett.*, 1970, **25**, 1430.
80 M. B. Maple, D. Wohlleben, *Phys. Rev. Lett.*, 1971, **27**, 511.
81 Y. Haga, J. Derr, A. Barla, B. Salce, G. Lapertot, I. Sheikin, K. Matsubayashi, N. K. Sato, J. Flouquet, *Phys. Rev. B,* 2004, **70**, 220406.
82 A. Jayaraman, E. Bucher, P. D. Dernier, L. D. Longinotti, *Phys. Rev. Lett.*, 1973, **31**, 700–703.
83 S. Ariponnammal, S. Chandrasekaran, *J. Nano- Electron. Phys.*, 2011, **3**, 529–535.
84 A.P. Menushenkov, R.V. Chernikov, V.V. Sidorov, K.V. Klementiev, P.A. Alekseev, A. V. Rybina, *JETP Lett.*, 2006, **84**, 119–123.
85 K. Imura, M. Saito, M. Kaneko, T. Ito, T. Hajiri, M. Matsunami, S. Kimura, K. Deguchi, H. S. Suzuki, N. K. Sato, *J. Phys.: Conf. Ser.*, 2015, **592**, 012028.
86 J. Arvanitidis, K. Papagelis, S. Margadonna, K. Prassides, A. N. Fitch, *Nature*, 2003, **425**, 599–602.
87 S. Margadonna, J. Arvanitidis, K. Papagelis, K. Prassides, *Chem. Mater.*, 2005 **17**, 4474-4478.
88 J. Arvanitidis, K. Papagelis, S. Margadonna, K. Prassides, *Dalton Trans.*, 2004, **19**, 3144-3146.
89 Z. X. Yin, X. Du, W. Z. Cao, J. Jiang, C. Chen, S. R. Duan, J. S. Zhou, X. Gu, R. Z. Xu, Q. Q. Zhang, W. X. Zhao, Y. D. Li, Y.-F. Yang, H. F. Yang, A. J. Liang, Z. K. Liu, H. Yao, Y. P. Qi, Y. L. Chen, and L. X. Yang, *Phys. Rev. B*, 2022, **105**, 245106.
90 H. Yamaoka, A. Ohmura, N. Tsujii, H. Ishii, N. Hiraoka, H. Sato, M. Sawada, *Phys. Rev. B*, 2024, **109**, 155147.
91 M. Hofmann, S. J. Campbell, A. V. J Edge, *J. Magn. Magn. Mater.*, 2004, **272**, E489-E490.
92 N. V. Musnikov, *Low Temp. Phys.* 2015, **41**, 946–964.
93 Z. E. Brubaker, R. L. Stillwell, P. Chow, Y. Xiao, C. Kenney-Benson, R. Ferry, D. Popov, S. B. Donald, P. Söderlind, D. J. Campbell, J. Paglione, K. Huang, R. E. Baumbach, R. J. Zieve, J. R. Jeffries, *Phys. Rev. B*, 2018, **98**, 214115. 8
94 I. L. Fedushkin, O. V. Maslova, E. V. Baranov, A. S. Shavyrin, *Inorg. Chem.*, 2009, **48**, 2355-2357.

95 I. L. Fedushkin, O. V. Maslova, A. G. Morozov, S. Dechert, S. Demeshko, F. Meyer, *Angew. Chem. Int. Ed.*, 2012, **51**, 10584-10587.
96 D. A. Lukina, A. A. Skatova, R. V. Rumyantcev, S. V. Demeshko, F. Meyer, I. L. Fedushkin, *Dalton Trans.*, 2024, **53**, 8850-8856.
97 S. L Selektor, A. V. Shokurov, V. V., Arslanov, Y. G. Gorbunova, K. P. Birin, O. A. Raitman, F. Morote, T. Cohen-Bouhacina, C. Grauby-Heywang, A. Y. Tsivadze, *J. Phys. Chem. C*, 2014, **118**, 4250-4258.
98 A. V. Shokurov, D. S. Kutsybala, A. G. Martynov, A. V. Bakirov, M.A. Shcherbina, S. N. Chvalun, Y. G. Gorbunova, A. Y. Tsidave, A. V. Zaytseva, D. Novikov, V. V. Arslanov, S. L. Selektor, *Langmuir*, 2020, **36**, 1423-1429.
99 I. Saiful, M. I. Hossain, K. Katoh, M. Yamashita, R. Arafune, S. M. Fakruddin Shahed, T. Komeda, *J. Phys. Chem. C*, 2022, **126**, 17152-17163.
100 M. Tricoire, N. Mahieu, T. Simler, G. Nocton, *Chem. – Eur. J.*, 2021, **27**, 6860-6879.
101 C. H. Booth, D. Kazhdan, E. L. Werkema, M. D. Walter, W. W. Lukens, E.D. Bauer, Y.-J. Hu, L. Maron, O. Eisenstein, M. Head-Gordon, R. A. Andersen, *J. Am. Chem. Soc.*, 2010, **132**, 17537-17549.
102 M. D. Walter, D. J. Berg, R. A. Andersen, *Organometallics*, 2006, **25**, 3228.
103 K. S. Pedersen, P. Perlepe, M. L. Aubrey, D. N. Woodruff, S. E. Reyes-Lillo, A. Reinholdt, L. Voigt, Z. Li, K. Borup, M. Rouzières, D. Samohvalov, F. Wilhelm, A. Rogalev, J. B. Neaton, J. R. Long, R. Clérac, *Nat. Chem.*, 2018, **10**, 1056–1061.
104 P. Perlepe, I. Oyarzabal, K. S. Pedersen, P. Negrier, D. Mondieig, M. Rouzières, E. A. Hillard, F. Wilhelm, A. Rogalev, E. A. Suturina, C. Mathonière, R. Clérac, *Polyhedron*, 2018, **153**, 248-253.
105 P. Perlepe, I. Oyarzabal, A. Mailman, M. Yquel, M. Platunov, I. Dovgaliuk, M. Rouzières, P. Négrier, D. Mondeig, E. S. Sututina, M.-A. Dourges, S. Bonhommeau, R. A. Musgrave, K. S. Pedersen, D. Chernyshov, F. Wilhelm, A. Rogalev, C. Mathonière, R. Clérac, *Science*, 2020, **370**, 587-592.
106 P. Perlepe, I. Oyarzabal, L. Voigt, M. Kubus, D. N. Woodruff, S. E. Reyes-Lillo, M. L. Aubrey, P. Négrier, M. Rouzières, F. Wilhelm, A. Rogalev, J. B. Neaton, J. R. Long, C. Mathonière, B. Vignolle, K. S. Pedersen, R. Clérac, *Nat. Commun.*, 2022, **13**, 5766.
107 M. Kubus, L. Voigt, K. S. Pedersen, *Inorg. Chem. Commun.*, 2020, **114**, 107819.
108 M. N. Bochkarev, I. L. Fedushkin, S. Dechert, A. A. Fagin, H. Schumann, *Angew. Chem. Int. Ed.*, 2001, **40**, 3176-3178.
109 W. J. Evans, T. S. Gummersheimer, J. W. Ziller *J. Am. Chem. Soc.* 1995, **117**, 8999–9002.
110 G. Heckmann, M. Niemeyer, *J. Am. Chem. Soc.* 2000, **122**, 4227–4228.
111 J. R. van den Hende, P. B. Hitchcock, S. A. Holmes, M. F. Lappert, W.-P. Leung, T. C. W. Mak, S. Prashar, *J. Chem. Soc., Dalton Trans.*, 1995, 1427-1433.
112 Z. Xie, K.-Y Chiu, B. Wu, T. C. W. Mak, *Inorg. Chem.* 1996, **35**, 5957–5958.
113 L. Voigt, M. Kubus, K. S. Pedersen, *Nat. Commun.*, **11**, 4705.
114 D. Écija, J. I. Urgel, A. C. Papgeorgiou, S. Joshi, W. Auwärter, A. P. Seitsonen, S. Klyatskaya, M. Ruben, S. Fischer, S. Vijayaraghavan, Joachim Reichert, J. V. Barth. *Proc. Natl Acad. Sci.*, 2013, **110**, 6678–6681.
115 J. J. Oppenheim, G. Skorupskii, M. Dincă, *Chem. Sci.*, 2020, **11**, 11094-11103.
116 V. Smetana, S. P. Kelley, A. V. Mudring, R. D. Rogers, *Sci. Adv.*, 2020, **6**, eaay7685.
117 T. Gorai, W. Schmitt, T. Gunnlaugsson, *Dalton Trans.*, 2021, **50**, 770-784.
118 Y. Zhang, S. Liu, Z.-S. Zhao, Z. Wang, R. Zhang, L. Liu, Z.-B. Han, *Inorg. Chem. Front.*, 2021, **8**, 590-619.
119 S. Sun, Y. Zhao, J. Wang, R. Pei, *J. Mater. Chem. B*, 2022,**10**, 9535-9564.
120 H. Chen, L. Voigt, M. Kubus, D. Mihrin, S. Mossin, R. W. Larsen, S. Kegnæs, S. Piligkos, K. S. Pedersen, *J. Am. Chem. Soc.* 2021, **143**, 14041–14045.
121 H. Chen, A. S. Manvell, M. Kubus, M. A. Dunstan, G. Lorusso, D. Gracia, M. S. B. Jørgensen, S. Kegnæs, F. Wilhelm, A. Rogalev, M. Evangelisti, K. S. Pedersen, *Chem. Commun.*, 2023, **59**, 1609-1612.
122 F. Guillou, A. K. Pathak, D. Paudyal, Y. Mudryk, F. Wilhelm, A. Rogalev, V. K. Pecharsky, *Nat. Commun.*, 2018, **9**, 2925.
123 Z. Mo, Q. Liu, W. Hao, L. Li, H. Xie, Q. Fu, X. Gao, J. Shen, *Mater. Today Phys.*, 2024, **41**, 101351.
124 A. S. Manvell, M. A. Dunstan, D. Gracia, J. Hrubý, M. Kubus, J. McPherson, E. Palacios, H. Weihe, S. Hill, J. Schnack, M. Evangelisti, K. S. Pedersen, *ChemRxiv*, 2024, DOI 10.26434/chemrxiv-2024-swrbm. This content is a preprint and has not been peer-reviewed.
125 M. A. Dunstan, A. S. Manvell, N. J. Yutronkie, F. Aribot, J. Bendix, A. Rogalev, K. S. Pedersen, *Nature Chem.* 2024, **16**, 735–740.
126 T. Wang, J. Lei, Y. Wang, L. Pang, F. Pan, K.-J. Chen, H. Wang, *Small*, 2022, **18**, 2203307.
127 C. Li, L. Zhang, J. Chen, X. Li, J. Sun, J. Zhu, X. Wang, Y. Fu, *Nanoscale*, 2021, **13**, 485-509.